Research Article | Vol. 25, No. 24 | 27 Nov 2017 | OPTICS EXPRESS 29934
Optics EXPRESS

Effect of crystalline family and orientation on stimulated Brillouin scattering in whispering-gallery mode resonators

SOULEYMANE DIALLO,[1] JEAN-PIERRE AUBRY,[1] AND YANNE K. CHEMBO[1,2,*]

[1] *FEMTO-ST Institute, Univ. Bourgogne Franche-Comté, CNRS, Optics Department, 15B Avenue des Montboucons, 25030 Besançon cedex, France*
[2] *Georgia Tech-CNRS Joint International Laboratory [UMI 2958], Atlanta Mirror Site, School of Electrical and Computer Engineering, 777 Atlantic Dr NW, Atlanta GA 30332, USA*
[*] *yanne.chembo@femto-st.fr*

Abstract: Ultra-high Q whispering-gallery mode resonators pumped by a continuous-wave laser are known to enhance stimulated Brillouin scattering when optimal resonance and phase-matching conditions are met. In crystalline resonators, this process depends critically on the crystal orientation and family, which impose the elastic constants defining the velocity of the acoustic waves. In this article, we investigate the effect of crystalline orientation and family on this velocity which is proportional to the Brillouin frequency down-shift. In particular, the study is based on the development of a model and numerical simulations of acoustic wave velocities that propagate along the periphery of four fluoride crystals, namely calcium, magnesium, lithium and barium fluoride. We find that depending on the crystal and its orientation, the frequency excursion around the Brillouin offset can vary from few tens of kHz to more than a GHz.

OCIS codes: (140.4780) Optical resonators; (260.1180) Crystal optics; (290.5900) Scattering, stimulated Brillouin; (350.4010) Microwaves.

References and links

1. D. V. Strekalov, C. Marquardt, A. B. Matsko, H. G. L. Schwefel and G. Leuchs, "Nonlinear and quantum optics with whispering gallery resonators," J. Opt. **18**, 123002 (2016).
2. G. Lin, S. Diallo, R. Henriet, M. Jacquot, and Y. K. Chembo, "Barium fluoride whispering-gallery-mode disk-resonator with one billion quality-factor," Opt. Lett **39**, 6009–6012 (2014).
3. I. S. Grudinin, V. S. Ilchenko, and L. Maleki, "Ultrahigh optical Q factors of crystalline resonators in the linear regime," Phys. Rev. A **74**, 063806 (2006).
4. A. Coillet, R. Henriet, K. P. Huy, M. Jacquot, L. Furfaro, I. Balakireva, L. Larger, and Y. K. Chembo, "Microwave photonics systems based on whispering-gallery-mode resonators," J. Vis. Exp **78**, e50423 (2013).
5. P. DelHaye, A. Schliesser, O. Arcizet, T. Wilken, R. Holzwarth, and T. J. Kippenberg, "Optical frequency comb generation from a monolithic microresonator," Nature **450**, 1214-1217 (2007).
6. S. B. Papp, P. DelHaye, and S. A. Diddams, "Mechanical control of a microrod-resonator optical frequency comb", Phys. Rev. X **3**, 031003 (2013).
7. S. M. Spillane, T. J. Kippenberg, and K. J. Vahala, "Ultralow-threshold raman laser using a spherical dielectric microcavity," Nature **415**, 621-623 (2002).
8. R. Henriet, G. Lin, A. Coillet, M. Jacquot, L. Furfaro, L. Larger, and Y. K. Chembo, "Kerr optical frequency comb generation in strontium fluoride whispering-gallery mode resonators with billion quality factor," Opt. Lett. **40**, 1567–1570 (2015).
9. K. Saleh and Y. K. Chembo, "On the phase noise performance of microwave and millimeter-wave signals generated with versatile Kerr optical frequency combs," Opt. Express **24**, 25043–25056 (2016).
10. K. Saleh, R. Henriet, S. Diallo, G. Lin, R Martinenghi, I. V. Balakireva, P. Salzenstein, A Coillet, and Y. K. Chembo, "Phase noise performance comparison between optoelectronic oscillators based on optical delay lines and whispering gallery mode resonators," Opt. Express **22**, 32158–32173 (2014).
11. K. Saleh, G. Lin, and Y. K. Chembo, "Effect of laser coupling and active stabilization on the phase noise performance of optoelectronic microwave oscillators based on whispering-gallery-mode resonators," IEEE Photon. J. **7**, 1–11 (2015).
12. K. Saleh and Y. K. Chembo, "Phase noise performance comparison between microwaves generated with Kerr optical frequency combs and optoelectronic oscillators," Electron. Lett. **53**, 264-265 (2017).

#307714 https://doi.org/10.1364/OE.25.029934
Journal © 2017 Received 22 Sep 2017; revised 30 Oct 2017; accepted 30 Oct 2017; published 15 Nov 2017

Optics EXPRESS

13. Y. K. Chembo, "Kerr optical frequency combs: theory, applications and perspectives," Nanophotonics **5**, 214–230 (2016).
14. S. Diallo, G. Lin, R. Martinenghi, L. Furfaro, M. Jacquot, and Y. K. Chembo, "Brillouin Lasing in Ultra-High Q Lithium Fluoride Disk-Resonators," IEEE Photon. Technol. Lett. **28**, 955–958 (2016).
15. G. Lin, S. Diallo, J. M. Dudley and Y. K. Chembo, "Universal scattering in ultra-high Q whispering gallery mode resonators," Opt. Express **24**, 14880 (2016).
16. I. S. Grudinin, A. B. Matsko and L. Maleki, "Brillouin lasing with a CaF_2 whispering gallery mode resonator," Phys. Rev. Lett. **102**, 043902 (2009).
17. G. P. Agrawal, *Nonlinear Fiber Optics* (Academic Press, 2007).
18. R. Boyd, *Nonlinear Optics* (Academic Press, 2003).
19. J. C. Beugnot, T. Sylvestre, D. Alasia, H. Maillotte, V. Laude, A. Monteville, L. Provino, N. Traynor, S. F. Mafang and L. Thevenaz, "Complete experimental characterization of stimulated Brillouin scattering in photonic crystal fiber," Opt. Express **15**, 15517–15522 (2007).
20. H. Lee, T. Chen, J. Li, K. Y. Yang, S. Jeon, O. Painter and K. J. Vahala, "Chemically etched ultrahigh-Q wedge-resonator on a silicon chip," Nat. Photonics **6**, 369–373 (2012).
21. J. Li, H. Lee, and K. J. Vahala, "Microwave synthesizer using an on-chip Brillouin oscillator," Nat. Commun. **4**, 2097 (2013).
22. J. Li, H. Lee, and K. J. Vahala, "Low-noise Brillouin laser on a chip at 1064 nm," Opt. Lett **39**, 287–290 (2014).
23. J. Li, M. G. Suh and K. Vahala, "Microresonator Brillouin gyroscope," Optica **4**, 346–348 (2017).
24. C. D. Cantrell, "Theory of nonlinear optics in dielectric spheres. III. Partial wave-index dependence of the gain for stimulated Brillouin scattering," J. Opt. Soc. Am. B **8**, 2181-2189 (1991).
25. S. C. Ching, P. T. Leung, and K. Young, "Spontaneous Brillouin scattering in a microdroplet," Phys. Rev. A **41**, 5026 (1990).
26. A. L. Huston, H. B. Lin, J. D. Eversole, and A. J. Campillo, "Nonlinear Mie scattering: electrostrictive coupling of light to droplet acoustic modes," Opt. Lett. **15**, 1176-1178 (1990).
27. H. M. Lai, P. T. Leung, C. K. Ng, and K Young, "Nonlinear elastic scattering of light from a microdroplet: role of electrostrictively generated acoustic vibrations," J. Opt. Soc. Am. B **10**, 924-932 (1993).
28. A. A. Savchenkov, A. B. Matsko, V. S. Ilchenko, D. Seidel, and L. Maleki, "Surface acoustic wave opto-mechanical oscillator and frequency comb generator," Opt. Lett. **36**, 3338-3340 (2011).
29. H. Shin, W. Qiu, R. Jarecki, J. A. Cox, R. H. Olsson III, A. Starbuck, Z. Wang, and P. T. Rakich, "Tailorable stimulated Brillouin scattering in nanoscale silicon waveguides," Nat. Commun. **4**, 1944 (2013).
30. W. Loh, J. Becker, D. C. Cole, A. Coillet, F. N. Baynes, S. B. Papp, and S. A. Diddams, "A microrod-resonator Brillouin laser with 240 Hz absolute linewidth," New J. Phys. **18**, 045001 (2016).
31. E. Dieulesaint and D. Royer, *Ondes Élastiques dans les Solides : Application au Traitement du Signal* (Masson, 1974).
32. B. A. Auld, *Acoustic Fields and Waves in Solids* (Krieger, 1990).
33. C. Kittel, *Introduction to Solid State Physics* (Wiley, 2004).
34. M. J. Weber, *Handbook of Optical Materials* (CRC Press, 2002).
35. V. Janovec, T. Hahn, H. Klapper, and J. Privratska, *International Tables for Crystallography. Volume D : Physical Properties of Crystals* (International Union of Crystallography and Kluwer Academic Publishers, 2003).
36. W. L. Bond, "The mathematics of the physical properties of crystals," Bell Syst. Tech. J. **22**, 1–72 (1943).
37. Y. K. Chembo, I. S. Grudinin, N. Yu, "Spatiotemporal dynamics of Kerr-Raman optical frequency combs," Phys. Rev. A **92**, 043818 (2015).
38. G. Lin and Y. K. Chembo, "Phase-locking transition in Raman combs generated with whispering gallery mode resonators," Opt. Lett. **41**, 3718–3721 (2016).
39. Y. K. Chembo, "Quantum dynamics of Kerr optical frequency combs below and above threshold: Spontaneous four-wave mixing, entanglement, and squeezed states of light," Phys. Rev. A **93**, 033820 (2016).

1. Introduction

The topic of light-matter interactions in ultra-high Q whispering gallery mode (WGM) resonators has gained significant attention in recent years (see for example [1] for a comprehensive review). WGM resonators have the capability to trap photons within their inner periphery for time durations that can exceed 1 μs, thereby leading to ultra-high quality (Q) factor values, typically in the 10^8–10^{11} range at 1550 nm. These resonators have small sizes (millimetric or sub-millimetric), support small mode volumes, and have been demonstrated in several types of materials [2–9]. They are useful as narrow linear filters in microwave photonics [10–12], but more interestingly, they also support various nonlinear effects at threshold powers inversely proportional to the square power of the Q-factor [13–16]. All these features are some of the reasons why WGM resonators have been for many years subject of intense research activities, and rapidly arose as an ideal platform to investigate nonlinear and quantum optics phenomena.

Optics EXPRESS

The light-matter interaction involving photons and acoustic phonons is Brillouin scattering, which has been extensively been investigated in optical fibers [17–19]. Stimulated Brillouin scattering (SBS) is a nonlinear phenomenon mediated by electrostriction. In fact, when the pump wave becomes intense in the medium through which it propagates, it interferes with the Stokes wave generated by spontaneous Brillouin scattering. The resulting beating creates by electrostriction an elastic wave that scatters back the pump. In WGM resonators, stimulated Brillouin scattering has allowed for various applications including high spectral purity microwave generation, lasers, and recently gyroscopes [20–23].

SBS has been observed in several architectures of WGM resonators [24–29]. With precise control of the resonator dimensions in order to match its Free Spectral Range (FSR) to the Brillouin induced shift, Lee *et al.* have demonstrated SBS in a silica WGM resonator on silicon chip with a record quality factor of 8.75×10^8 [20]. In 2013, Li *et al.* have demonstrated microwave synthesis based on cascaded Brillouin scattering with record phase noise floor of −160 dBc/Hz [21]. In their work, they used the photo-detection of the 1st and 3rd Stokes in order to generate microwave signals at frequencies of 10.8 GHz and 21.7 GHz. Another interesting result has been obtained by Loh *et al.*, who demonstrated a Brillouin laser with a linewidth of 240 Hz [30]. All the performances cited previously have been obtained with amorphous WGM resonators. The first observation of SBS in a crystalline resonator has been reported by Grudinin *et al.* with a 5 mm diameter calcium fluoride (CaF_2) WGM resonator [16]. The reported scattering process has been observed at a laser pump wavelength of 1064 nm, a threshold power of 5 μW and a Stokes wave down-shifted 17.7 GHz away from the pump. Recently, Lin *et al.* have evidenced high-order cascaded Brillouin Stokes generation ranging from 8.2 to 49 GHz, using a millimetric barium fluoride (BaF_2) crystalline WGM resonator pumped at 1550 nm with few tens of milliwatts. SBS has also been reported in a lithium fluoride WGM resonator [14].

Millimetric crystalline resonators, particularly those manufactured with metal difluorides, present very interesting features for microwave photonics. First of all, ultra-high Q factors beyond 10^9 are achievable [2, 3]. The Brillouin shift at 1550 nm and their FSR have the same order of magnitude, which is in the X, K or Ka Band, and leads to the possibility to generate high-spectral purity microwave signals. However, to date and to the best of our knowledge, beyond the quality factor and the material the crystal is made of, there is not another selection criteria that allows to state which fluoride crystal is more suitable for the exploitation of SBS in crystalline WGM resonators, depending on the targeted application. The purpose of the present theoretical study is to answer to this question by studying the behavior of the acoustic waves responsible of Brillouin scattering in crystalline resonators. More precisely, we investigate the importance of the orientation and family of the crystal on the Brillouin amplification bandwith by developping a model that tracks the velocity of acoustic waves which lead to the Brillouin offset frequency within the inner periphery of any given crystal.

The article is organized as follows. In the next section, we will first present the model used to calculate the acoustic wave velocity leading to the Brillouin frequency down-shift. We then use this model to determine numerically the Brillouin offset variation for four fluoride crystals, namely CaF_2, BaF_2, MgF_2 and LiF. The last section concludes the article.

2. Acoustic wave velocity and Brillouin shift in crystalline WGM resonators

2.1. Acoustic wave velocity in a given orientation

The velocity of acoustic waves that propagate along a crystalline WGM resonator may vary in a nontrivial way that requires attention. In fact, the Brillouin amplification process depends on the Brillouin offset frequency $\nu_B = 2nV_a/\lambda$, where n is the crystal refractive index, λ the laser wavelength and V_a the acoustic wave velocity. This amplification process has a bandwith $\Delta\nu_B$ that distributes the acoustic energy and contributes to the Stokes waves linewidth broadening,

Optics EXPRESS

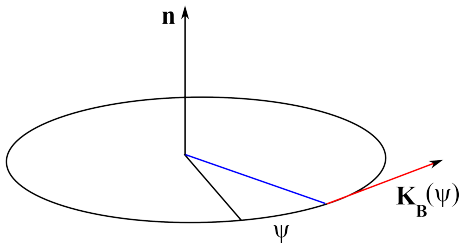

Fig. 1. Illustration of the normal vector **n** and angle ψ characterizing the propagation of the acoustic wave in the plan of the crystalline WGM disk.

following:

$$\frac{\Delta\nu_B}{\nu_B} = \frac{\nu_B^{max} - \nu_B^{min}}{\nu_B} = \frac{V_a^{max} - V_a^{min}}{V_a}. \tag{1}$$

It appears clearly that minimizing the acoustic waves velocity variation leads to reduced Brillouin amplification bandwidth, therefore, narrow Stokes waves linewidth. This minimization can be achieved by a careful selection of the WGM resonator material. In fact, as illustrated in Fig. 1, the acoustic wave velocity varies along the disk periphery according to the orientation of his wave vector $\mathbf{K_B}$ which is colinear to the pump wave vector $\mathbf{K_P}$. Otherwise, the crystals used in this work are monocrystalline and anisotropic. They are ordered set of atoms and their properties can be described by tensors [31]. When applied to an anisotropic crystal, a strain characterized by strain tensor T_{ij} and leads to deformations characterized by the deformation tensor S_{kl}. These tensors are linked by the well known Hooke's law [31–34], expressed by:

$$T_{ij} = c_{ijkl} S_{kl}, \tag{2}$$

where c_{ijkl} represents the crystal elastic constants. Other important parameters in the characterization of a crystal are his family and normal direction. Simple cuts characterized by a normal along the z, y, and x axis are respectively denoted [001], [010], [100] and in that order called z-, y- and x-cut. A more complex cut with the normal in the xyz plan exists under the name of [111] orientation. The four mentioned crystalline orientations are illustrated in Fig. 2. The structure and family of the crystal give its elastic constants which lead to the acoustic wave velocity using wave propagation equation.

A plane wave propagating in any direction $\mathbf{n}(n_1, n_2, n_3)$ of a given material induces a displacement field $\mathbf{u}(u_1, u_2, u_3)$, which has a spatial and temporal dependency that will depend on the intracavity constraints. The equation of motion can be written as

$$\rho \frac{\partial u_i^2}{\partial t^2} = \frac{\partial T_{ij}}{\partial x_j}, \tag{3}$$

where T_{ij} is the strain tensor, and ρ the volumetric mass density of the crystal. By inserting Hooke's law of Eq. (2) in Eq. (3), one obtains the dynamical equation:

$$\rho \frac{\partial^2 u_i}{\partial t^2} = c_{ijkl} \frac{\partial^2 u_l}{\partial x_j \partial x_k} \tag{4}$$

for the displacement field **u**. The coefficients i, j, k, l vary from 1 to 3, and therefore, the solutions of this equation are three plane waves that can be written as:

$$u_i = U_i \, f\left(t - \frac{n_i x_i}{V}\right), \tag{5}$$

Optics EXPRESS

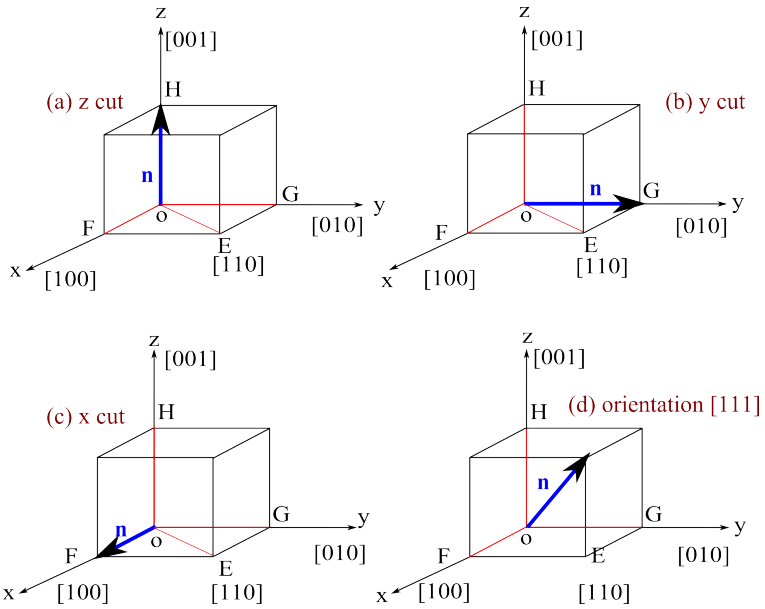

Fig. 2. Illustration of the orientation of a crystal as a function of the direction of its normal vector **n**. Figures (a), (b), and (c) correspond respectively to so-called z-cut, y-cut and x-cut, while (d) correspond to the [111] orientation.

where f is a scalar function, and V is the acoustic wave velocity. If we insert this solution in Eq. (4), we obtain the well known Christoffel equation [31–33]

$$\rho V^2 U_i = c_{ijkl} n_j n_k U_l \,, \tag{6}$$

where n_j and n_k are the projections of the propagation direction **n**. From here, one can introduce the second order tensor Γ also known as Christoffel tensor, following

$$\Gamma_{il} = c_{ijkl} n_j n_k \,. \tag{7}$$

Considering its symmetry, ($\Gamma_{ij} = \Gamma_{ji}$), the tensor Γ_{ij} has only six distinct terms amongst nine. For a wave in a given polarization, the Christoffel equation becomes:

$$(\Gamma_{il} - \rho V^2 \delta_{il})\, U_l = 0 \tag{8}$$

and admits non-trivial solutions only if the so-called Christoffel determinant defined below is null:

$$|\Gamma_{il} - \rho V^2 \delta_{il}| = 0 \,. \tag{9}$$

The resolution of this equation shows the existance of three waves that propagate simultaneously in the crystal [35]. One amongst them is longitudinal and is responsible of stimulated Brillouin scattering, while the two others are transverse [31–33]. This equation can be simplified using the symmetries of the system and the Voigt notation for which $c_{ijkl} \equiv C_{\alpha\beta}$, with the index reductions $11 \rightarrow 1$, $22 \rightarrow 2$, $33 \rightarrow 3$, $23 \equiv 32 \rightarrow 4$, $13 \equiv 31 \rightarrow 5$, and $12 \equiv 21 \rightarrow 6$. Hence, the

Optics EXPRESS

developpement of Eq. (9), also known as secular equation, leads to the following expressions:

$$\Gamma_{11} = C_{11}n_1^2 + C_{66}n_2^2 + C_{55}n_3^2 + 2C_{16}n_1n_2 + 2C_{15}n_1n_3 + 2C_{56}n_2n_3 \quad (10)$$

$$\Gamma_{22} = C_{66}n_1^2 + C_{22}n_2^2 + C_{44}n_3^2 + 2C_{26}n_1n_2 + 2C_{46}n_1n_3 + 2C_{24}n_2n_3 \quad (11)$$

$$\Gamma_{33} = C_{55}n_1^2 + C_{44}n_2^2 + C_{33}n_3^2 + 2C_{45}n_1n_2 + 2C_{35}n_1n_3 + 2C_{34}n_2n_3 \quad (12)$$

$$\Gamma_{12} = C_{16}n_1^2 + C_{26}n_2^2 + C_{45}n_3^2 + (C_{12} + C_{66})n_1n_2 + (C_{14} + C_{56})n_1n_3 + (C_{46} + C_{25})n_2n_3 \quad (13)$$

$$\Gamma_{13} = C_{15}n_1^2 + C_{46}n_2^2 + C_{55}n_3^2 + (C_{14} + C_{56})n_1n_2 + (C_{13} + C_{55})n_1n_3 + (C_{36} + C_{45})n_2n_3 \quad (14)$$

$$\Gamma_{23} = C_{65}n_1^2 + C_{24}n_2^2 + C_{43}n_3^2 + (C_{46} + C_{25})n_1n_2 + (C_{36} + C_{45})n_1n_3 + (C_{23} + C_{44})n_2n_3\,. \quad (15)$$

If for example we consider a cubic crystal, the matrix of elastic constants can be explicitly written as:

$$[\mathbf{C}_{\alpha\beta}] = \begin{bmatrix} C_{11} & C_{12} & C_{12} & 0 & 0 & 0 \\ C_{12} & C_{11} & C_{12} & 0 & 0 & 0 \\ C_{12} & C_{12} & C_{11} & 0 & 0 & 0 \\ 0 & 0 & 0 & C_{44} & 0 & 0 \\ 0 & 0 & 0 & 0 & C_{44} & 0 \\ 0 & 0 & 0 & 0 & 0 & C_{44} \end{bmatrix}, \quad (16)$$

so that the Christoffel tensor terms for this crystal become

$$\Gamma_{11} = C_{11}n_1^2 + C_{44}(n_2^2 + n_3^2) \quad (17)$$

$$\Gamma_{12} = \Gamma_{21} = (C_{12} + C_{44})n_1n_2 \quad (18)$$

$$\Gamma_{13} = \Gamma_{31} = (C_{12} + C_{44})n_1n_3 \quad (19)$$

$$\Gamma_{22} = C_{44}(n_1^2 + n_3^2) + C_{11}n_2^2 \quad (20)$$

$$\Gamma_{23} = \Gamma_{32} = (C_{12} + C_{44})n_2n_3 \quad (21)$$

$$\Gamma_{33} = C_{44}(n_1^2 + n_2^2) + C_{11}n_3^2\,. \quad (22)$$

For a wave propagating in the [100] direction (along Ox_1), Christoffel determinant is:

$$\begin{vmatrix} C_{11} - \rho V^2 & 0 & 0 \\ 0 & C_{44} - \rho V^2 & 0 \\ 0 & 0 & C_{44} - \rho V^2 \end{vmatrix} = 0\,. \quad (23)$$

From this expression, one can deduce the longitudinal acoustic wave velocity V_{L} polarized along [100] and the two transverse waves $V_{\mathrm{T}_{1,2}}$ respectively polarized along [010] and any vector normal to the [100] direction following:

$$V_{\mathrm{L}} = \sqrt{\frac{C_{11}}{\rho}}, \qquad V_{\mathrm{T}_1} = \sqrt{\frac{C_{44}}{\rho}}, \qquad V_{\mathrm{T}_2} = \sqrt{\frac{C_{44}}{\rho}}\,. \quad (24)$$

For a propagation in [110] direction, Christoffel determinant is rather:

$$\begin{vmatrix} \frac{1}{2}(C_{11} + C_{44}) - \rho V^2 & \frac{1}{2}(C_{11} + C_{44}) & 0 \\ \frac{1}{2}(C_{12} + C_{44}) & \frac{1}{2}(C_{11} + C_{44}) - \rho V^2 & 0 \\ 0 & 0 & C_{44} - \rho V^2 \end{vmatrix} = 0\,. \quad (25)$$

Optics EXPRESS

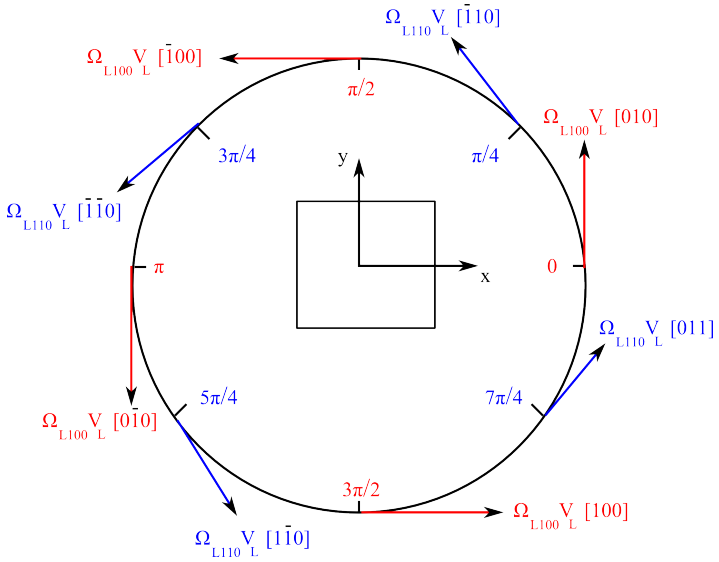

Fig. 3. Illustration of the longitudinal acoustic waves velocities V_{L} and corresponding Brillouin sifts Ω_{L} for particular directions, in accordance with longitudinal acoustic wave velocities expressions given by Eq. (26), and for a crystal oriented along [001] which corresponds to a z-cut.

Using the same approach mentioned previously, one can calculate from this determinant the expression of the longitudinal wave velocity V_{L} polarized along [110] and the two transverse waves velocities $V_{\mathrm{T}_{1,2}}$ polarized respectively along [101] and [011]:

$$V_{\mathrm{L}} = \sqrt{\frac{C_{11} + C_{12} + 2C_{44}}{2\rho}}, \qquad V_{\mathrm{T}_1} = \sqrt{\frac{C_{11} - C_{12}}{2\rho}}, \qquad V_{\mathrm{T}_2} = \sqrt{\frac{C_{44}}{\rho}}. \tag{26}$$

The two examples developed in Eqs. (24) and (26) unveil the mechanism behind the periodic variation of the acoustic wave velocity. For instance, the acoustic wave along [100] direction will have a longitudinal component expressed by $V_L = \sqrt{C_{11}/\rho}$ with a peridocicity of $\pi/2$, colinear to the optical wave vector. For a propagation along [110] direction, the longitudinal acoustic wave velocity expressed by $V_L = \sqrt{(C_{11} + C_{12} + 2C_{44})/2\rho}$ will have a periodicity $\pi/2$ colinear to the optical wave vector in those particular points as illustrated in Fig. 3. However, apart from these particular directions, one expects the variations of wave velocity and frequency along the disk periphery. Moreover, these variations are necessarily periodic, since they depend on the angle ψ between the acoustic wave vector and the the crystal plan axis. It therefore becomes important to develop a systematic method to calculate the acoustic wave velocity $V(\psi)$ and frequency $\nu_{\mathrm{B}}(\psi)$ along the disk periphery. For this purpose, the starting point is the calculation of the crystal elastic constants in the rotated plane, as explained in the next subsection.

2.2. *Elastic coefficients in the rotated plane: elastic rotation matrices*

The tensor or matrix approach is generally used to calculate with the elastic and strain coefficients. The main goal of these approaches is to obtain a simple expression that links strain and elasticity using Hooke's law. An alternative method, introduced by Bond [36], uses instead a 6×6 matrix approach that transforms strain and elastic coefficients in any desired system of coordinates [32]. The constraint field T_{ij} transforms to T'_{ij}=$a_{ik}a_{jl}T_{kl}$ by a change of system coordinates where $i, j, k, l \in \{1, 2, 3\}$ correspond to the axes x, y, z, and a_{mn} to the cosine directors of the new system

Optics EXPRESS

of coordinates. The developement of the constraints field T'_{xx} leads to the following equation:

$$\begin{aligned} T'_{xx} = \quad & a_{xx}^2 T_{xx} + a_{xx}a_{xy}T_{xy} + a_{xx}a_{xz}T_{xz} \\ & + a_{xy}a_{zx}T_{yx} + a_{xy}^2 T_{yy} + a_{xy}a_{xz}T_{yz} \\ & + a_{xz}a_{xx}T_{zx} + a_{xz}a_{xy}T_{zy} + a_{xz}^2 T_{zz} \quad , \end{aligned} \tag{27}$$

and similar expressions for the other coefficients T_{uv}. Since the strain field is symetric ($T_{ij} = T_{ji}$), Eq. (27) can actually be reduced to:

$$T'_{xx} = a_{xx}^2 T_{xx} + a_{xy}^2 T_{yy} + a_{xz}^2 T_{zz} + 2a_{xx}a_{xy}T_{xy} + 2a_{xx}a_{xz}T_{xz} + 2a_{xy}a_{xz}T_{yz}\,, \tag{28}$$

or equivalently, to

$$T'_1 = a_{xx}^2 T_1 + a_{xy}^2 T_2 + a_{xz}^2 T_3 + 2a_{xx}a_{xy}T_6 + 2a_{xx}a_{xz}T_5 + 2a_{xy}a_{xz}T_4. \tag{29}$$

using Voigt notation.

Using the same approach for the 9 components of $[\mathbf{T}']$, we have $T'_H = M_{HI}T_I$ with $H, I = 1, 2, 3, 4, 5, 6$. Analogously, we obtain the strain matrix by introducing $S'_{ij} = a_{ik}a_{jl}S_{kl}$, expressed in reduced notation by $S'_K = N_{KJ}S_J$ where the indices K and J vary form 1 to 6. The 6×6 rotation matrices $[\mathbf{M}]$ and $[\mathbf{N}]$ can now be explicitly expressed as

$$[\mathbf{M}] = \begin{bmatrix} [\mathbf{B_1}] & 2[\mathbf{B_2}] \\ [\mathbf{B_3}] & [\mathbf{B_4}] \end{bmatrix} \quad \text{and} \quad [\mathbf{N}] = \begin{bmatrix} [\mathbf{B_1}] & [\mathbf{B_2}] \\ 2[\mathbf{B_3}] & [\mathbf{B_4}] \end{bmatrix} \tag{30}$$

where the intermediate matrices

$$[\mathbf{B_1}] = \begin{bmatrix} a_{xx}^2 & a_{xy}^2 & a_{xz}^2 \\ a_{yx}^2 & a_{yy}^2 & a_{yz}^2 \\ a_{zx}^2 & a_{zy}^2 & a_{zz}^2 \end{bmatrix} \tag{31}$$

$$[\mathbf{B_2}] = \begin{bmatrix} a_{xy}a_{xz} & a_{xz}a_{xx} & a_{xx}a_{xy} \\ a_{yy}a_{yz} & a_{yz}a_{yx} & a_{yx}a_{yy} \\ a_{zy}a_{zz} & a_{zz}a_{zx} & a_{zx}a_{zy} \end{bmatrix} \tag{32}$$

$$[\mathbf{B_3}] = \begin{bmatrix} a_{yx}a_{zx} & a_{yy}a_{zy} & a_{yz}a_{zz} \\ a_{zx}a_{xx} & a_{zy}a_{xy} & a_{zz}a_{xz} \\ a_{xx}a_{yx} & a_{xy}a_{yy} & a_{xz}a_{yz} \end{bmatrix} \tag{33}$$

$$[\mathbf{B_4}] = \begin{bmatrix} a_{yy}a_{zz} + a_{yz}a_{zy} & a_{yx}a_{zz} + a_{yz}a_{zx} & a_{yy}a_{zx} + a_{yx}a_{zy} \\ a_{xy}a_{zx} + a_{xz}a_{zy} & a_{xz}a_{zx} + a_{xx}a_{zz} & a_{xx}a_{zy} + a_{xy}a_{zx} \\ a_{xy}a_{yz} + a_{xz}a_{yy} & a_{xz}a_{yx} + a_{xx}a_{yz} & a_{xx}a_{yy} + a_{xy}a_{yx} \end{bmatrix} \tag{34}$$

are only introduced here for the sake of notation conciseness. These coefficients reported in Hooke's law lead to $[\mathbf{T}'] = [\mathbf{M}][\mathbf{T}] = [\mathbf{M}][\mathbf{C}][\mathbf{S}]$, and since $[\mathbf{S}] = [\mathbf{N}]^{-1}[\mathbf{S}']$, one obtains $[\mathbf{T}'] = [\mathbf{M}][\mathbf{C}][\mathbf{N}]^{-1}[\mathbf{S}'] = [\mathbf{C}'][\mathbf{S}']$, so that

$$[\mathbf{C}'] = [\mathbf{M}][\mathbf{C}][\mathbf{N}]^{-1}\,. \tag{35}$$

The cosine director matrix inverse is equal to its transposed: $[\mathbf{a}]^{-1} = [\mathbf{a}]^{\mathbf{T}}$. Hence, if the matrix $[\mathbf{N}]$ is based on the cosine director matrix $[\mathbf{a}]$, the matrix $[\mathbf{N}]^{-1}$ corresponds to the matrix $[\mathbf{a}]^{-1}$, itself equal to its transposed. Therefore, $[\mathbf{N}]^{-1} = [\mathbf{M}]^{\mathbf{T}}$ and the expression of the elastic coefficients in the rotated plane is then:

$$[\mathbf{C}'] = [\mathbf{M}][\mathbf{C}][\mathbf{M}]^{\mathbf{T}}\,. \tag{36}$$

As explained in the next section, the determination of these rotation matrices permits to compute the acoustic wave velocity and Brillouin shift in WGM resonators.

Optics EXPRESS

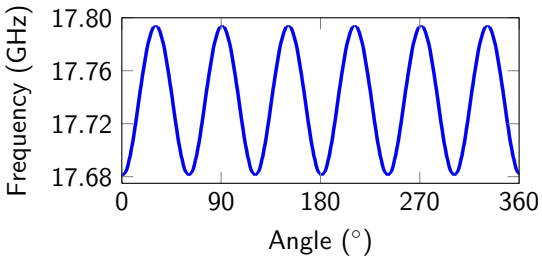

Fig. 4. Longitudinal acoustic mode frequency variations along the periphery of CaF_2 oriented along [111] at a wavelength of 1064 nm. The calculation reveals a longitudinal acoustic mode at a frequency of 17.7 GHz with a peak-to-peak frequency variation along the disk of 112 MHz. This is in agreement with the results reported by Grudinin *et al.* in [16].

3. Numerical simulations for fluorite WGM resonators

3.1. Step-by-step procedure

We propose a procedure of 10 steps to calculate acoustic waves velocities and Brillouin frequency shifts at any point along the crystalline WGM resonator. This methodology is based on formalisms introduced in the previous section, and they enable to investigate photon-phonon coupling underlying stimulated Brillouin scattering.

The ten steps of the method are the following: *(i)* Select the crystalline material (CaF_2, BaF_2, MgF_2, LiF, ...) and identify its elastic constants. *(ii)* Select a crystalline orientation for the disk under consideration ([100], [110], [111], etc); *(iii)* Express the coordinate changes using the rotation matrix **[M]**; *(iv)* Express the elastic coefficients matrix in the rotated plane using Eq. (36); *(v)* Choose a propagation direction for the acoustic wave in the disk plan and express the propagation vector coordinates **n** in this same plan; *(vi)* Define the Christoffel matrix for each value of the angle ψ (characterizing the propagation direction of the acoustic wave in the disk plan and presented in Fig. 1) using the Christofel equation given by Eq. (8); *(vii)* Determine the characteristics of the acoustic waves in any point of the disk periphery; *(viii)* Determine, as a function of ψ, the propagation direction of the acoustic wave in the disk plan, as well as the eigenvalues and eigenvectors of the matrix obtained previously – note that this calculation is performed using the Christofel determinant given by Eq. (8); *(ix)* Identify the longitudinal and transverse waves velocities; *(x)* Determine the Brillouin offset frequency generated by the longitudinal waves of the selected disk with the selected pump wavelength.

The validity of this procedure is tested hereafter by considering Brillouin scattering in fluorite crystals.

3.2. Results

A first task to test the validity of the procedure outlined above has been to compare its predictions with some results that have been published in recent years in the area of Brillouin scattering in crystalline WGM resonators. Indeed, one of the most important contribution along that line was provided by Grudinin, Matsko and Maleki in [16], where they had simulated the Brillouin offset frequency induced by the longitudinal acoustic mode propagating along the periphery of a [111]-oriented CaF_2 WGM resonator, pumped at a wavelength of 1064 nm. Our calculations of the Brillouin offset have been compared theirs in the same crystal, orientation and laser pump wavelength, and the result is displayed in Fig. 4. In full agreement with the results of Grudinin *et al.*, our calculations indicate that the Brillouin offset frequency is equal to 17.7 GHz, with a peak-to-peak dispersion along the disk periphery of approximately 112 MHz.

We have then simulated and compared the longitudinal and transversal acoustic modes of four

Optics EXPRESS

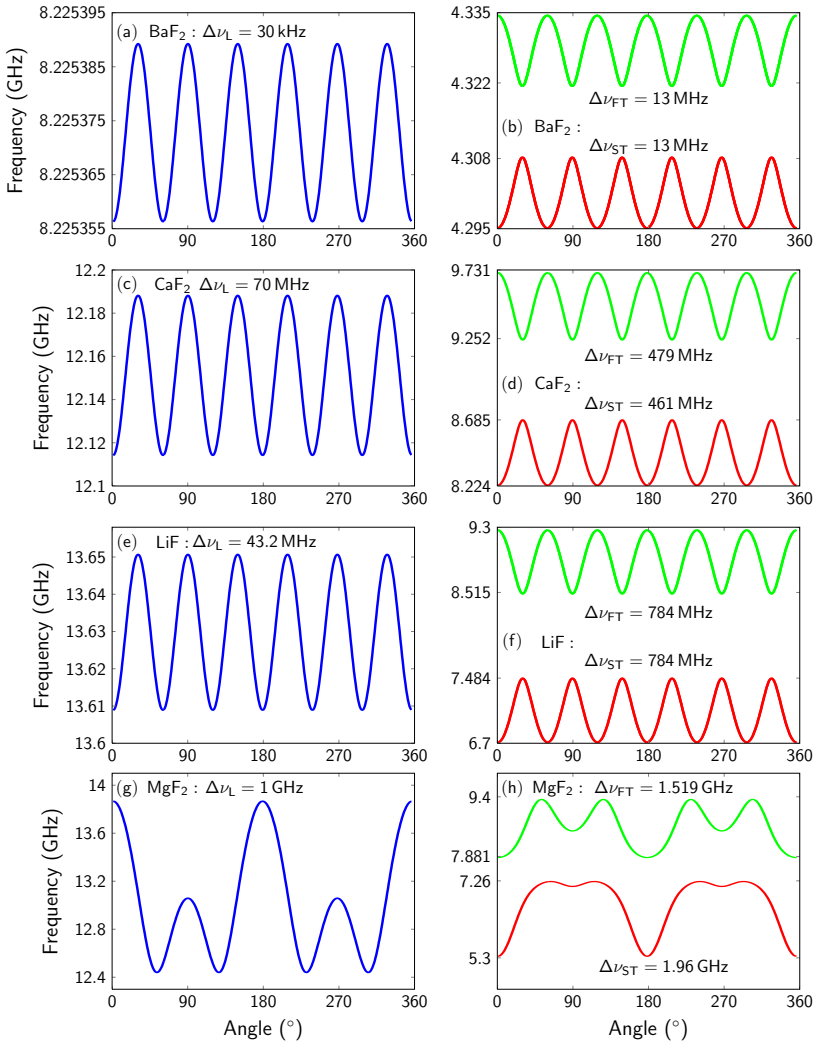

Fig. 5. Numerical simulations for the Brillouin shifts at 1550 nm, for different crystals oriented along [111]. Figures (a), (c), (e), and (g) (in blue) correspond respectively to transverse longitudinal acoustic waves for a crystal of BaF_2, CaF_2, LiF, and MgF_2. Figures (b), (d), (f), (h) represent respectively the fast transverse acoustic waves (or FT, in green) and slow transverse acoustic waves (or ST, in red) for the aforementioned crystals.

different fluoride crystals, namely BaF_2, CaF_2, LiF and MgF_2, all oriented along [111]. The results of these simulations at a wavelength of 1550 nm are presented in Fig. 5. One can monitor the Brillouin frequency variation for the longitudinal wave, and identify the crystal that minimize this variation.

The simulations results are summarized in Table 1. We observe that barium fluoride presents the smallest frequency variation, calculated at 30 kHz for a Brillouin offset frequency equal to 8.22 GHz. Calcium fluoride and lithium fluoride present respectively a frequency variation of 43.2 MHz and 70 MHz for their Brillouin offsets at 12.15 GHz and 13.61 GHz. Magnesium fluoride presents an important frequency variation of 1 GHz, with a complex profile structure for its longitudinal mode. It therefore appears that barium fluoride oriented along [111] seems to

Optics EXPRESS

Table 1. Summary of longitudinal Brillouin frequency shifts f_L, fast transverses f_{FT} and slow transverses f_{ST} with their respective variations $\Delta\nu_L$, $\Delta\nu_{FT}$, $\Delta\nu_{ST}$, for ψ ranging from 0 to 2π, and for the following crystals in the [111] orientation: BaF_2, CaF_2, LiF, MgF_2. The laser pump wavelength is 1550 nm.

Crystal	**BaF_2**	**LiF**	**CaF_2**	**MgF_2**
f_L (GHz)	8.225	[13.61−13.65]	[12.11 - 12.19]	[12.4 - 13.8]
$\Delta\nu_L$ (MHz)	0.03	43.2	70	1000
f_{FT} (GHz)	[4.322 - 4.335]	[8.515 - 9.3]	[9.252 - 9.731]	[7.881 - 9.4]
$\Delta\nu_{FT}$ (MHz)	13	784	479	1519
f_{ST} (GHz)	[4.295 - 4.308]	[6.7 - 7.484]	[8.224 - 8.685]	[5.3 - 7.26]
$\Delta\nu_{ST}$ (MHz)	13	784	461	1960

be a very promising configuration for the investigation of SBS in crystalline whispering gallery mode resonators, whenever the smallest linewidths are highly desirable.

It should be emphasized that at the experimental level, the acoustic wave velocity critically depends on the crystal density and rotated elastic coefficient. Local perturbations have an influence on acoustic wave velocity, energy dissipation and scattering energy, therefore impacting as well the Brillouin offset frequency. It is therefore important to stress the need for optimizing the fabrication techniques of these crystalline resonators. Characterization techniques such as X-Ray orientation could for example allow to identify large crystalline defects. High Resolution X-Ray Diffraction could help to identify local crystalline perturbations. Infrared, ultraviolet and chemical analysis could evidence material impurities while classical X-ray diffraction could allow to characterize the crystalline structure of the resonator.

4. Conclusion

We have developed a systematic procedure that permits to calculate the velocity of an acoustic wave that propagates along the inner periphery of a crystalline whispering-gallery mode disk-resonator. Such waves are responsible of Brillouin scattering, and we have highlighted the importance of crystalline orientation and family on the stability of the Brillouin shift frequency. We have shown that the frequency deviation can be as low as few tens of kHz, such as in [111]-oriented BaF_2. We however emphasize that beyond crystal orientation, stimulated Brillouin scattering depends on several optical properties (attenuation, scattering, etc.), but also on the acoustic Q-factor and on the phonon intracavity dynamics. We hope that this study will allow to explore in depth the proven potential of crystalline WGM resonators as a platform for low-power, versatile photon-phonon interactions, in view of microwave photonics applications such as microwave generation or compact gyroscopes, just to name a few. Future investigations will be devoted as well to the understanding of the effects of crystal and molecular symmetries on Raman interactions [37, 38], as well as at the photon-phonon interactions at the single-quantum level in WGM resonators [39].

Funding

European Research Council (ERC) (StG 278616) & Versyt (PoC 632108); *Centre National d'Etudes Spatiales* (CNES) SHYRO; *Région de Franche-Comté* CORPS; Université de Franche-Comté SYOCUS; Labex ACTION; Labex FIRST-TF.